ELSEVIER

Contents lists available at ScienceDirect

Journal of Power Sources

journal homepage: www.elsevier.com/locate/jpowsour



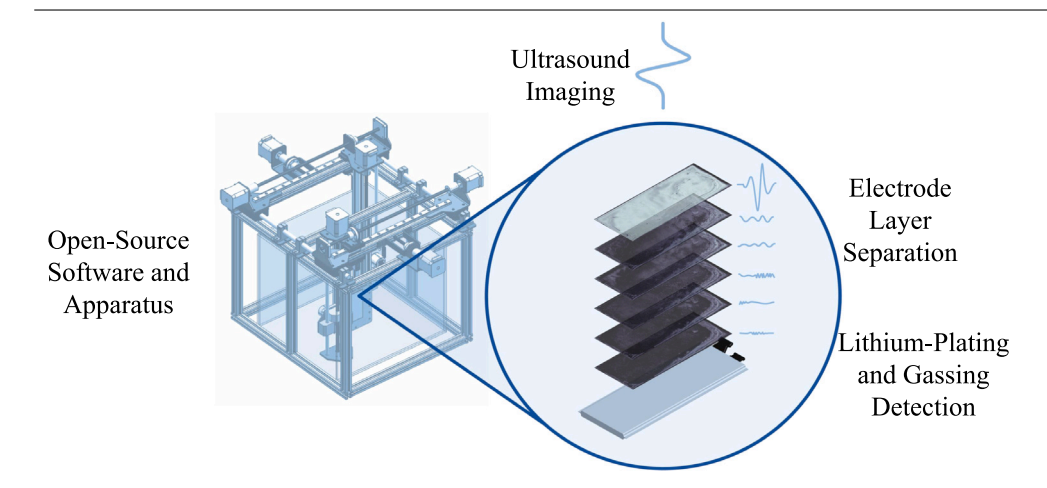


In situ tomography of lithium-ion battery cells enabled by scanning acoustic imaging

David Wasylowski ^{a,c,*}, Sven Neubauer ^a, Matthias Faber ^{a,c}, Heinrich Ditler ^{a,c}, Morian Sonnet ^{a,c}, Alexander Blömeke ^{a,c}, Philipp Dechent ^{a,c}, Alexander Gitis ^{a,e}, Dirk Uwe Sauer ^{a,b,c,d}

- ^a Chair for Electrochemical Energy Conversion and Storage Systems, Institute for Power Electronics and Electrical Drives (ISEA), RWTH Aachen University, Campus-Boulevard 89, 52074 Aachen, Germany
- b Institute for Power Generation and Storage Systems (PGS), E.ON ERC, RWTH Aachen University, Mathieustrasse 10, 52074 Aachen, Germany
- ^c Jülich Aachen Research Alliance, JARA-Energy, Templergraben 55, 52056 Aachen, Germany
- d Helmholtz Institute Münster (HI MS), IEK 12, Forschungszentrum Jülich, 52425 Jülich, Germany
- e Safion GmbH, Tempelhofer Str. 12, 52068 Aachen, Germany

GRAPHICAL ABSTRACT



HIGHLIGHTS

- · Electrode layer separation achieved with ultrasound imaging.
- · In Situ and cost-effective measurement method.
- · Gas formation and Lithium-Plating detectable.
- · Ultrasound images verified with a post-mortem examination.

ARTICLE INFO

ABSTRACT

Keywords: Ultrasound Imaging the interior of battery cells provides vital information for battery manufacturing, as well as lifetime and performance prediction. This work demonstrates a scalable and in-situ method to image the structural

E-mail address: david.wasylowski@isea.rwth-aachen.de (D. Wasylowski).

URL: https://www.isea.rwth-aachen.de (D. Wasylowski).

https://doi.org/10.1016/j.jpowsour.2023.233295

Received 3 April 2023; Received in revised form 18 May 2023; Accepted 4 June 2023 Available online 15 June 2023

0378-7753/© 2023 The Author(s). Published by Elsevier B.V. This is an open access article under the CC BY-NC-ND license (http://creativecommons.org/licenses/by-nc-nd/4.0/).

^{*} Corresponding author at: Chair for Electrochemical Energy Conversion and Storage Systems, Institute for Power Electronics and Electrical Drives (ISEA), RWTH Aachen University, Campus-Boulevard 89, 52074 Aachen, Germany.

Lithium plating Scanning acoustic microscopy Tomography Signal processing state of battery cells with layer resolution. Building on our prior publication, we apply ultrasound waves on pouch cells and process the reflected instead of the transmitted wave. This allows us to utilize time-of-flight data to provide depth information for later signal parts. We develop and demonstrate an algorithm that dissects the reflected ultrasound wave and calculates individual reflections from material interfaces within the electrode stack by fitting their estimated envelopes onto the Hilbert transformation of the entire wave. Consecutive individual reflections are used to calculate the reflection coefficient from the material interface, which is then mapped onto a color map. Using this algorithm, we image an aged and pristine pouch cell from the same manufacturing batch. The generated images showed a clear correlation with optical images from a post-mortem analysis. Indications from the ultrasound image were verified as lithium-plating.

1. Introduction

Due to the adoption of electric vehicles and an expansion of grid storage, a battery market of about 2.5 TWh/year is forecasted for 2030 [1]. To meet the global demand for battery cells, it is necessary to reduce battery cell prices while increasing performance [2]. This requires adjustments in the production chain and on the material level, aiming to increase the production throughput without reducing the product quality [3]. Therefore, cell manufacturers must ensure that when developing new cell types or adapting production steps, a product is made that meets all relevant criteria. For this purpose, test scenarios are carried out under different loads and environmental conditions [4]. In order to keep the scope of these test series small and the results conclusive, non-destructive imaging techniques are necessary to detect possible defects or accelerated aging phenomena during the test run without having to perform cell disassembly [5]. In particular, nondestructive imaging techniques can identify structural changes that are not detectable by electrical testing [6].

Different methods exist for conducting non-destructive imaging, such as computed tomography (CT), magnetic resonance imaging (MRI), pulse thermography, and neutron-based characterization methods, each possessing its own set of strengths and weaknesses [7-10]. Although some of these technologies are promising for a quality assurance process, the main disadvantages are that they are challenging to include in a production line, require high financial resources, or even specially trained personnel on-site for X-ray methods (radiation safety officers). Furthermore, most of these technologies are not able to detect gas formation. To overcome these disadvantages, much effort has been spent in recent years exploring the applicability of ultrasonic measurement methods in the field of lithium-ion batteries. Ultrasonic diagnosis traditionally has many applications in the medical field and industrial flaw detection, where relatively macroscopic and homogeneous test specimens are present (down to millimeter scale). Thus, transfer to thinfilm inhomogeneous battery materials (down to micrometer scale) is not immediately trivial [11].

The first battery-related publications in the field of ultrasound imaging date back to 2019. In publications by Deng et al. from that year, the wetting of lithium-ion pouch cells was investigated using a method called scanning acoustic microscopy (SAM) and a commercial acoustic microscope. This allowed a 2D representation of the cell to be made and highlighted which parts of the battery cell have increased electrolyte concentration than others [12,13].

In our own previous publication, the SAM technique was used to image lithium plating and gassing caused by production defects in 2D [14]. Here, a resolution of about 500 micrometers could be demonstrated by a self-developed and open hardware apparatus. In a publication by Bauermann et al. [15], the SAM method was extended for the first time to achieve some depth-related information. By dividing the signal into time-equivalent sections and analyzing those sections separately, Bauermann et al. were able to visualize indications that are not only present on the surface of the cell. Unfortunately, because of the static decomposition of the ultrasound signal, this technique was yet unable to assign the ultrasound information to a specific depth of the cell, i.e., a layer, ultimately leading to no clear separation between indications inside the cell. Furthermore, a commercial acoustic microscope and

software were used in the publication, which leads to a lack of technical details on signal processing. Additionally, the high cost of such a device impedes market penetration and therefore does not take advantage of the low cost of the measurement methodology. Furthermore, S. Feiler et al. recently presented a measurement setup that can extract the average Young's modulus of the entire electrode stack in the center of the cell dimensions. Although this quantitative method is an excellent addition to the emerging imaging methods, it lacks spatial resolution. It cannot measure the aging phenomena not captured by the fixed sensors, especially aging in the outer edges of electrode sheets [16].

It is, therefore, of interest to explore a low-cost apparatus with which depth resolution can be achieved and meaningful images can be generated. In the following, a setup from our previous publication is extended with a method that allows ultrasound images with meaningful depth resolution. To accomplish this, all indications from the electrodes are extracted from the ultrasound data and assigned to the corresponding electrode. We therefore have a layer-specific depth resolution. This method is illustrated and used to non-destructively image aging phenomena in a commercial lithium-ion cell. The images are then compared with those of a pristine cell. The focus of this work is to present a tool and its possibilities for future publications in this field. To accomplish this, all relevant underlying effects that occur during the experiments are analyzed to demonstrate the diagnostic capabilities of the framework.

2. Experimental setup

To apply ultrasonic waves on cells, a setup already published by us was used. For a detailed description of the setup, please refer to [14]. The setup consists of two movable measuring arms to which ultrasonic transducers are attached. The measuring arms are independent so that both can be moved synchronously or asynchronously with a speed of up to 600 mm/s. With the setup, it is possible to perform ultrasonic measurements in the so-called pitch-catch as well as in the pulse-echo mode. In pitch-catch mode, two transducers are positioned opposite of each other, and the sample is placed in between them. One transducer always serves as the ultrasound emitter, and the other always as the receiver. In pulse-echo mode, only one transducer is used, serving as both emitter and receiver. After emitting the ultrasound, a serially connected switch switches so that the reflected wave can be sampled with an analog-to-digital converter (ADC), thus changing the function of the emitter to that of a receiver. In pulse-echo mode, one of the two measuring arms in the device is neglected accordingly. The apparatus is depicted in Fig. 1(a) and 1(b).

In recent literature, it has been suggested that the cumulative reflected signal at the receiving transducer consists of a linear combination of smaller partial waves [17,18]. These partial waves are generated by the reflection and transmission of the wave at each material transition (anode/cathode/separator). The ratio of the reflected and transmitted part of the wave largely depends on the ratio of the acoustic impedance. The transmitted part of the wave propagates further through the cell until it encounters the next material transition, where partial transmission and reflection take place again until the opposite cell surface is hit again. To make the spatial resolution of such material transitions as high as possible, it is necessary to use a transducer with high frequency and bandwidth. This leads to a compact ultrasonic pulse in

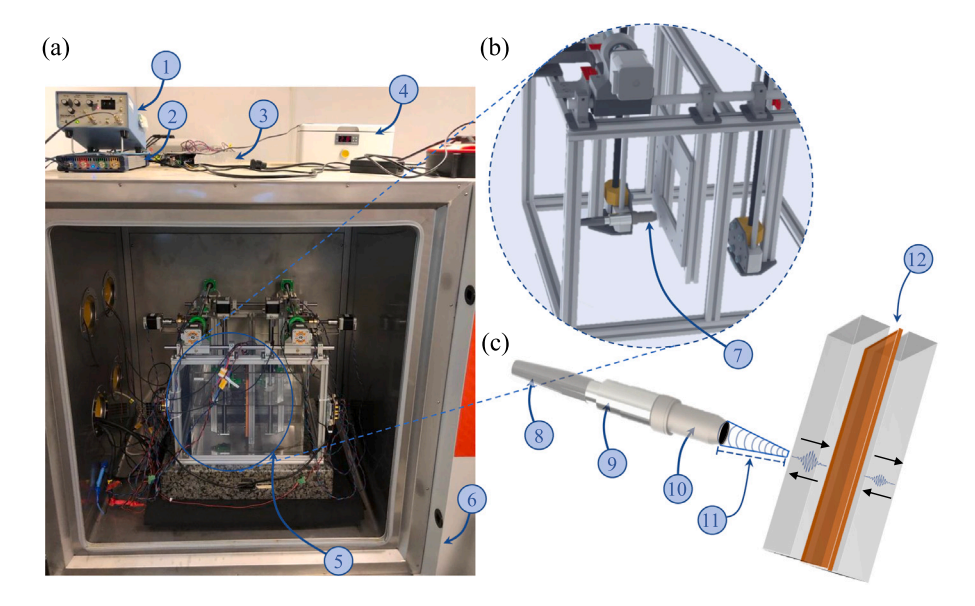


Fig. 1. Experimental setup and measurement method. (a): Developed measuring apparatus with ultrasonic pulser (1) Picoscope (2), switching power supply for voltage supply to the stepper motors (3), temperature monitoring and emergency stop (4), measuring apparatus (5) and temperature chamber (6). (b): Zoom to the developed apparatus with adapted submersion transducer Olympus V324 (7) with a frequency of 25 MHz and bandwidth of 60%. (c): Rendering of the selected transducer consisting of a BNC cable (8), a waterproof connector (9), and the submersion transducer (10). The point-focusing effect is schematically shown in (11). The focal point distance is about 3.8 cm. In (12), a schematic representation of a double-coated anode is shown. It is visualized how transmissions and reflections of the emitted ultrasonic wave partially occur at material transitions.

the time and space domain [15]. In our setup, we use the Olympus V324 transducer with a frequency of 25 MHz and a bandwidth of about 60%. Since the setup is immersed in a silicone oil with a wateridentical viscosity of 1 cSt, a so-called submersion transducer is used. These have a quarter wavelength matching layer adapted to water, which significantly compensates the reflected wave at the transition from the sensor into the liquid medium resulting in less destructive interference and more energy in the emitted wave. In contrast to our previous publication, point-focused transducers were used. This leads to a smaller beam diameter at the focal point and, thus, to a higher maximum resolution. The focusing effect is simplified in Fig. 1(c). In the context of this work, measurements are recorded with a spatial resolution 250 µm. The maximum possible resolutions are described in [14]. Preliminary analysis has shown that a higher resolution does not contribute to more information from the sample. This might change with more optimized transducer setups in the future. The depth resolution is mainly limited by the wavelength of the ultrasound wave which can be calculated using the sound frequency and speed to a value of about 200 µm. Since the wavelength is in the order of magnitude of a stack of an andode-, cathode- and separatorsheet it is not possible to increase the depth resolution without significantly sacrificing the number of electrodes layers which can be imaged.

3. Methods

3.1. Preliminary aging tests

The battery cells in our experiments are commercial lithium-ion pouch battery cells manufactured by Kokam Co., Ltd., Suwon, Republic of Korea. Kokam classifies these cells with the model number SLPB065070180 as ultra-high energy batteries with a nominal capacity of 11.6 Ah and an energy density of 246 Wh/kg. This battery model has both tabs on the same side. Internally, the cell stack consists of 17 anode and 16 cathode layers double-coated with an additional single-coated cathode layer both on the top and bottom. In-house material analyses using inductively coupled plasma atomic emission spectroscopy (ICP-AES) and energy-dispersive X-ray spectroscopy (EDX) show that the negative electrode's active material is graphite, and the positive electrode's active material is a nickel-rich lithium nickel

manganese cobalt oxide (NMC) with a stoichiometric ratio of Ni:Mn:Co of 15:1:2.

The cells have been aged at a temperature of 25 °C with a CC-CV charge at a C-rate of 1C and a CC discharge at 1C as well. The voltage limits were according to the datasheet. Additionally, the cells have been clamped with a constant force of 50 kPa. This has been enabled by using four springs with a spring constant of 15.7 N/mm manufactured by Seitz Normteile GmbH and two pressure plates made of copper with the dimensions: $67 \times 165 \times 19.5$ mm (WxLxH). There are 18 mm deep drill holes inside the pressure plate to embed temperature sensors. There are additional temperature sensors at the cell tabs. The clamping setup is displayed in Fig. 2(a). The resulting aging trajectory is displayed in Fig. 2(b). Up until approximately 1000 full cycles, the cell shows almost completely linear aging. At around 200 equivalent full cycles, the residual capacity rises slightly. This effect is most likely due to the so-called passive electrode effect, where lithium migrates from the anode overhang, causing the capacity to rise [19]. After 1000 cycles, the residual capacity decreases rapidly. According to the datasheet, the nominal cycle life of the cell is at least 3000 cycles without any clamping. Since clamping is the only thing that differs from the datasheet conditions, it is of interest to study the internal structural changes that may have led to accelerated aging. For this purpose, the clamped cells are relaxed in preparation for the ultrasound evaluation. They are then fixated into an aluminum profile at the seams to be embedded upright into the setup. For the ultrasound investigation, one cell was selected from the aging series. The examination of the aging of all cells is part of a publication and will not be discussed further here. During the ultrasound investigation, the SoC of the battery cell is kept constant to prevent the acoustic impedance from changing due to the de/lithiation of the electrodes.

3.2. Signal processing

Compared to medical test objects, battery cells are a great challenge for acoustic tomography due to their increased sound velocity, attenuation, and thin-layered structure [18]. As motivated in Section 2, each material interface (i.e., between two electrode layers) with different acoustic impedances (Z_1 and Z_2) causes a partial reflection and a transmission of the ultrasound wave (primary reflection or transmission),

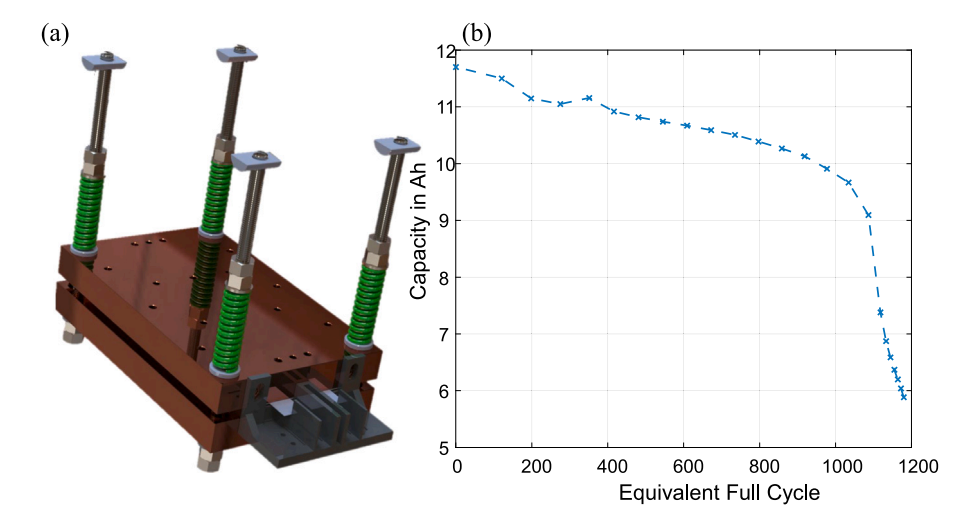


Fig. 2. Aging process for the Kokam SLPB065070180 cell under consideration. (a) Represents the measurement setup. This consists of 2 copper plates, which exert a constant force tension of 50 kPa with springs, and a contacting unit. (b) Depicts the aging trajectory of the cell at a temperature of 25 °C and 100 % DoD cycling at 1C. The aging process enters the so-called kneepoint at about 1100 equivalent full cycles.

which then themselves can be reflected and transmitted at the next interface (secondary reflection or transmission) This effect is visualized in Fig. 1(c). The reflected (A_r) and transmitted (A_t) wave amplitudes at each material interface are described by the following equations.

$$A_r = \left(\frac{Z_2 - Z_1}{Z_1 + Z_2}\right) A_i \tag{1}$$

$$A_t = \left(\frac{2Z_2}{Z_1 + Z_2}\right) A_i,\tag{2}$$

with

$$Z_i = \rho_i \left(K_i + \frac{4}{3} G_i \right)$$
 with $i = 1, 2$. (3)

Here K_i and G_i are the compression and shear moduli, respectively, which can be calculated from the modulus of elasticity E_i using Poisson's ratio, and ρ_i the density (for i = 1, 2). For macroscopic test specimens, it is sufficient to plot the absolute value of the total reflected ultrasonic wave over time and to map a spatial depth resolution with the information of the sound velocity [20]. The closer material transitions in test objects are to each other, the more likely the partial reflections are to overlap, given a finite bandwidth of the sound wave. To compute images that show the inner structure of the battery cell, it is, therefore, necessary to deconvolute the reflected signal. Additionally, Deng et al. suggested that electrolyte content significantly affects the acoustic impedance of materials [21]. In their recent publication, Feiler et al. calculated the effective Young's modulus of the same cell type used in our experiments to be 6.1 GPa at 0 % SoC and fully wetted with electrolyte [16]. On the other Hand Xu et al. calculated the Young's modulus of unwetted NMC to be 140 GPa. Additionally, Qi et al. calculated the Young's modulus of unwetted graphite anodes to be 32.47 GPa at the same SoC [22] while Gor et al. measured the Young's Modulus of the separator to be 247 MPa [23]. Considering the rule of mixture, we can therefore assume that the ultrasound transmission of both electrodes and the separator is significantly impacted by the electrolyte content [24] since the wet cell has significantly different Young's moduli compared to the dry electrodes and separator. Therefore it is safe to assume that the most significant reflections are taking place at the transition to the current collectors, which by design are not able to be wetted by electrolyte and have a constant Young's modulus of 130 GPa for copper [25] and 70 GPa for aluminum [26]. Therefore we view the stack of one anode coating, the separator, and the cathode coating as one "slice" for each layer. The procedure that we developed to try and achieve this will now be presented.

The impulse that the ultrasound transducer emits can be mathematically approximated with a wavelet [17]. It has been suggested that

each reflected wave has the shape of a wavelet as well [17]. Due to cell geometry, a new sound wave part arrives at the transducer before the previous one has decayed. Therefore it is necessary to calculate the original wavelets from the superimposition. So far, the effect of interferences in ultrasound measurements of lithium-ion batteries has not been fully explored. Thus it is unclear whether the amplitudes of the wavelets add up or subtract each other. Also, the exact travel time of the reflected waves becomes challenging to determine exactly since the speed of sound and wavelength change at material interfaces. The time of flight in between two battery layers correlates with the local coating thickness and therefore varies as well. Modeling these effects is subject to current research.

In addition to the superimposition of the wavelets, it must also be considered that the individual battery layers age largely independently of each other. It can therefore happen that two layers on top of each other are aged differently at the same x- and y-position. This principle is visualized in Fig. 3(a). This leads to the fact that the measured sound amplitude alone cannot be used to determine whether a deeper layer has an aging or defect-induced structural artifact or not. The reason is that sound is reflected stronger at aged or defect spots in the battery than at pristine ones due to the higher acoustic impedance (see Eq. (1)). However, a change in the reflection amplitude implies a change in the transmission amplitude, as well [14]. This results in different signal intensities at the two locations for the healthy lower battery layer. This would initially suggest that the second layer also has structural differences at the respective positions, which is, by design, not correct. In order to overcome these challenges, signal processing is split into two subtasks. Firstly, the reflected wavelets of each layer are computed from the entire reflected wave. After that, an algorithm calculates the pixel value for each reflection and, therefore, layer, which will now be referred to as a "slice".

3.2.1. Calculation of partial reflections

Intuitively the wavelet transformation seems to be suitable for the first subtask. This transformation compares the similarity between a so-called mother wavelet (or reference wavelet) and the measured wave signal [14]. The impulse of the ultrasound transducer given in the datasheet would serve as the base for the reference wavelet in this case. Besides the parameterization of the reference wavelet, there are multiple other challenges within signal processing. The frequencies of the reflected wavelets change, as well as their duration. The reason behind this is not yet fully understood, but Huang et al. claim that the signals are influenced by slight changes in the eigenfrequency between two electrodes [27]. This would lead to a non-linear runtime

of the algorithm because all parameters of the wavelet transformation have to be adapted for each targeted reflection. Therefore we use a different approach. Instead of observing high-frequency wavelets, their envelopes are fit to the envelope of the measured data. The main advantage of this method is the decreased computational effort required. The envelope of the measured signal can be described as the absolute value of the Hilbert transformation [28]. Moreover, this envelope can be approximated by a gaussian function, reducing the complexity of the method even further [29]. For this reason, the algorithm calculates one gaussian curve for every ultrasound reflection happening inside the battery cell. After that, each gaussian function is multiplied with the measured signal. This acts like a window function that nearly cancels out all values outside of the three-sigma-environment around a targeted wavelet. The function also weights the sample values in order to consider the overlapping of ultrasound reflections. As the first reflection does not overlap with a previous one, it needs to be taken into account that approximately the first half of the signal shall not be weighted.

$$G(x) = \exp\left(-\frac{(x-\mu)^2}{2 \cdot \sigma^2}\right) \tag{4}$$

Eq. (4) describes the gaussian envelopes. To construct these envelopes, two parameters need to be identified: The mean μ and the standard deviation σ . The mean value is the sampled value at each local maximum in the absolute Hilbert transformation. For the standard deviation, it needs to be taken into account that the durations of partial reflections differ. Since it is not possible to measure the exact σ with overlapping reflections, it has to be approximated. We do that by looking for a local minimum near the three-sigma-environment of the approximated bell curve from the data sheet. It will be later shown that this approximation is sufficient. The algorithm stops looking for reflections once the amplitude of the envelope drops below a certain threshold. This is usually the case after six reflections. For the overall algorithm, this results in a linear run time.

Finally, the procedure is visualized in Fig. 3(b) and (c). It becomes clear that the algorithm has now decomposed the original measurement into multiple wavelets. Each one of these makes up for a new reflection and, therefore, a pixel for each slice. When reassembling the decomposed signal and comparing it to the original measurement, it can be seen that the approximation error is tolerable (Fig. 3(c)). The RMS-values of the reconstructed and the original wave differ by 1.8% while only using four wavelets for reconstruction. In Section 4, we will use six wavelets for reconstruction, decreasing the RMSE even further.

3.2.2. Visualization of slices

In the next step, the algorithm computes pixel values for each reflection. As the calculations are applied to every measurement of the scan, the output is multiple slices that indicate different depths inside the battery. According to Section 3.2.1, these depths should correlate to the battery layers.

The literature has yet to reveal standardization regarding the calculation of pixel values. A common approach is to map the root-mean-squared- (RMS-)value of a single wavelet to a color map. According to Weinzierl, this effective value is proportional to the sound intensity [30]. However, the intensity does not consider the problem mentioned above, where upper battery layers influence the ultrasound signal of lower ones. To try and overcome this challenge, we propose a method where we calculate the reflection coefficients at each electrode, according to Eq. (1)–(3). These coefficients should ideally be independent of each other because they are only influenced by the material transition at each individual electrode surface, assuming similar eigenfrequencies [27]. The first reflection (surface layer reflection) can be easily calculated using Eq. (1) and solving for $A_r/A_i = \Gamma_i$, where i refers to the reflection number (in this case, 1 for the surface layer). The following reflection can be obtained by calculating the reflection

coefficient from the transmitted ultrasound wave between the first and second layer:

$$A_{\mathbf{r}} = \Gamma_2 \cdot \left(1 - \Gamma_1^2\right) \cdot A_{\mathbf{i}} \tag{5}$$

Considering the number of reflections and transmissions for a specific layer, all reflection coefficients can be calculated in a recursive formula. In this work, only primary reflections flow into the computation. The formula for each reflection coefficient Γ_i can be derived from the mentioned correlations and is presented in Eq. (6).

$$\Gamma_i = \frac{A_{\mathbf{r},i}}{A_i} \cdot \prod_{j=1}^{i-1} \frac{1}{\left(1 - \Gamma_j^2\right)} \tag{6}$$

Since the calculation of deeper reflections is recursively based on the previous ones, any errors from the previous ones add up, so deeper layers may result in distorted images. Additionally, the signal amplitude decreases due to attenuation at deeper layers. This must be taken into account when interpreting deeper slices. Finally, applying the two equations from above to every measurement of the data set results in multiple images, one for each battery slice.

4. Results

4.1. Images of the aged cell

The images for the evaluation of the algorithm show a total of six different slices inside the battery, which aim to resemble the first six battery layers. As demonstrated in Section 3.2.1, only about six layers can be imaged with sufficient signal-to-noise ratio since the ultrasonic wave is almost entirely attenuated by then with current sensor parameters. Since the attenuation of ultrasonic waves depends mainly on their frequency, one could resolve deeper layers with lower acoustic frequency. However, this will come at the expense of lower spatial resolution and sensitivity due to the higher wavelength. Another option to increase the depth penetration is to use higher voltage pulse excitation, leading to linearly higher wave amplitudes. Since this work focuses on presenting the methodology, which is transferable to both options without restrictions, we shall stick to a presentation of six layers in this work. First, the aged cell is presented, and after that, a pristine one of the same manufacturing batch. All ultrasound images are compared to the optical images, which were taken after the ultrasound evaluation and disassembly in a glove box using a flatbed scanner (Canon CanoScan LiDE 300). All images are mapped against the 'bone' color map. A selection of the most significant similarities between the ultrasound and optical images is marked in yellow. We start the analysis with the first slice (see Fig. 4). Since only a few pixel values are low and the other values are similar to each other, the first slice appears bright. A visual comparison between the first ultrasound slice and the first battery layer from the post-mortem analysis (consisting of the cell housing (not shown in Layer 1) and the backside of the first singlecoated cathode) reveals a significant resemblance, which confirms the design of this part of the algorithm. The first layer of the backside of the cathode sheet is displayed in (b). Besides the structures in the first ultrasound slice, which most likely resemble the housing, there is a bright indication marked by an ellipse. During cell disassembly, a wrinkle in the separator covering the first cathode sheet was visible. The mark of the wrinkle is still visible in layer 1 of the aluminum foil on the backside of the first single-coated cathode sheet (marked by an ellipse).

The following slices are dominated by a bright L-shaped structure in the top left corner (marked by a polygon). As will be discussed in the post-mortem analysis, there was a gas bubble there. This was confirmed by optical analysis of the cell housing (see supplementary material). Since high-frequency ultrasound is strongly attenuated by gas, any indications under the gas bubble will be difficult to image. Furthermore, the reflected ultrasound wave at the areas of the gas

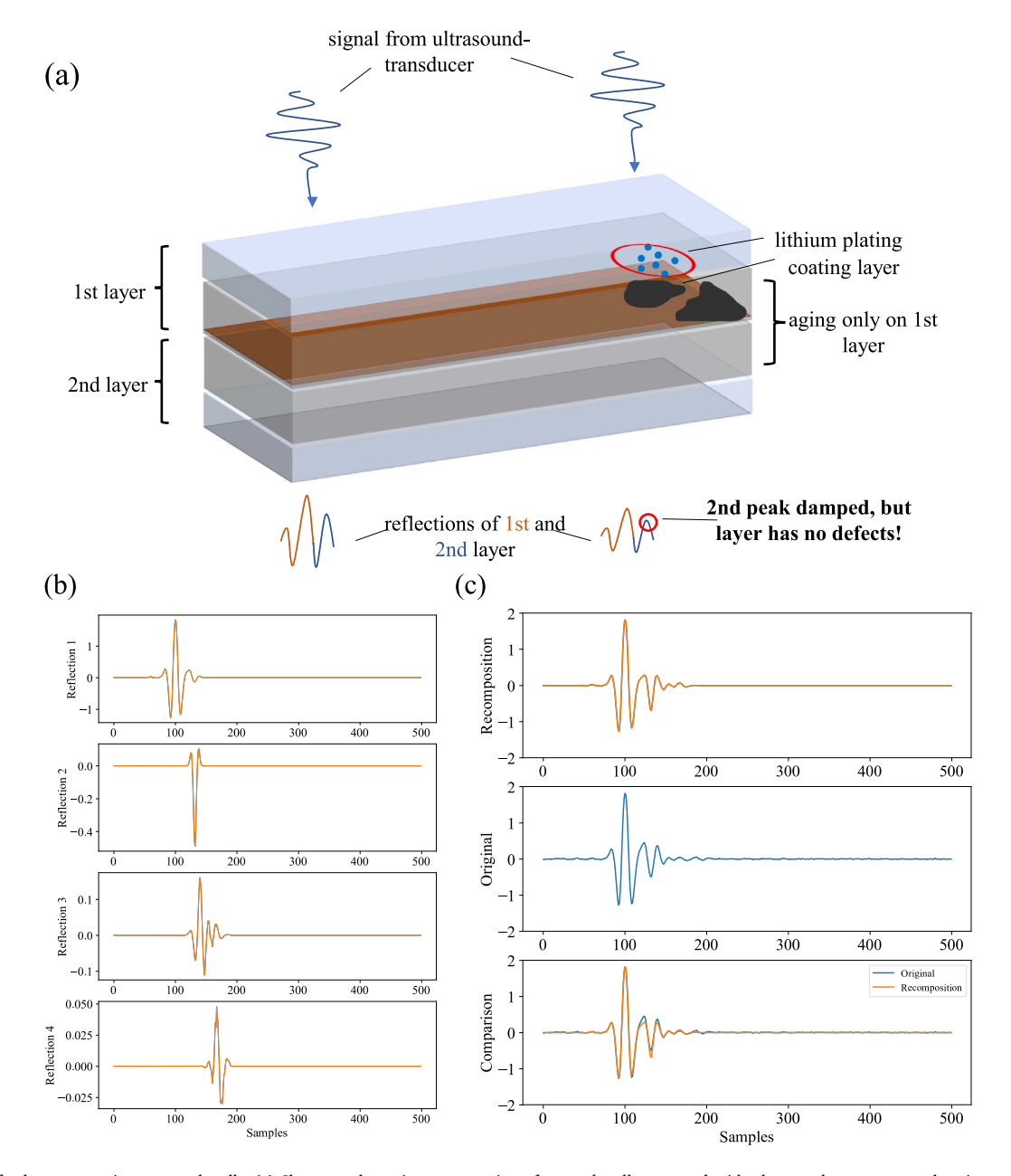


Fig. 3. Method for layer separation on pouch cells. (a) Shows a schematic representation of a pouch cell, measured with ultrasound waves at two locations, with an indication at only one of the two locations. As shown in the drawing below, effects on the upper layer must be considered for an adequate representation of deeper layers. (b) Shows the decomposition of the total ultrasound signal into four individual reflections, which correlate with the first four layers. (c) Shows the comparison of the recomposition with the original signal. The RMS-values of the reconstructed and the original wave differ by 1.8%. With an increasing number of calculated reflections, the difference decreases.

bubble showed clear differences to the wave at the areas with no gas bubble. The amplitude of the acoustic response with gas bag is smaller. However, the attenuation of the amplitude in the case of the gas bag is obviously much smaller, indicating different mechanical properties at this point. This also explains why the L-shaped indication of the gas ash was seen on each slice in Fig. 4: in this case, the altered acoustic response was interpreted as reflections from the individual layers. Thus, as a method of analyzing the images, if a structure is present almost identically in all slices, it could be assumed to be a gas bag. Additionally to the gas bubble, there seems to be a covering layer of a similar shape. As will be discussed in the post-mortem analysis, this covering layer is lithium-plating, which most probably caused the gassing.

Moreover, aging can be seen at the locations of the current collectors. There is also an S-shape visible on Layer three and four of the optical images (marked in blue). Unfortunately, we were not able to image those structures with the proposed method. Therefore, we adapted the algorithm for calculation of pixel values and instead of calculating the reflection coefficient (see Eq. (6)), we determine the absolute value of the difference of two consecutive partial reflections. Based on the adapted method we were able to image the S-shaped structures but with limited sensitivity to other effects. This caused by the exponential attenuation of the wave which is now no longer compensated by the calculation of the reflection coefficient. The corresponding images are depicted in the supplementary material. Unlike the gas bubble, this shape does not go on in the deeper layers indicating that the layers actually show different structures. Finally, a blurred pattern is visible in the center of most electrode slices. This pattern can also be recognized in the optical images from the post-mortem analysis (indicated by the zoom). As will be shown in the post-mortem analysis, the blurred pattern resembles spots of lithium-plating, but to a much lesser extend compared to the L-shaped structure in the top left. This shows that ultrasound can be used to detect the formation of gas

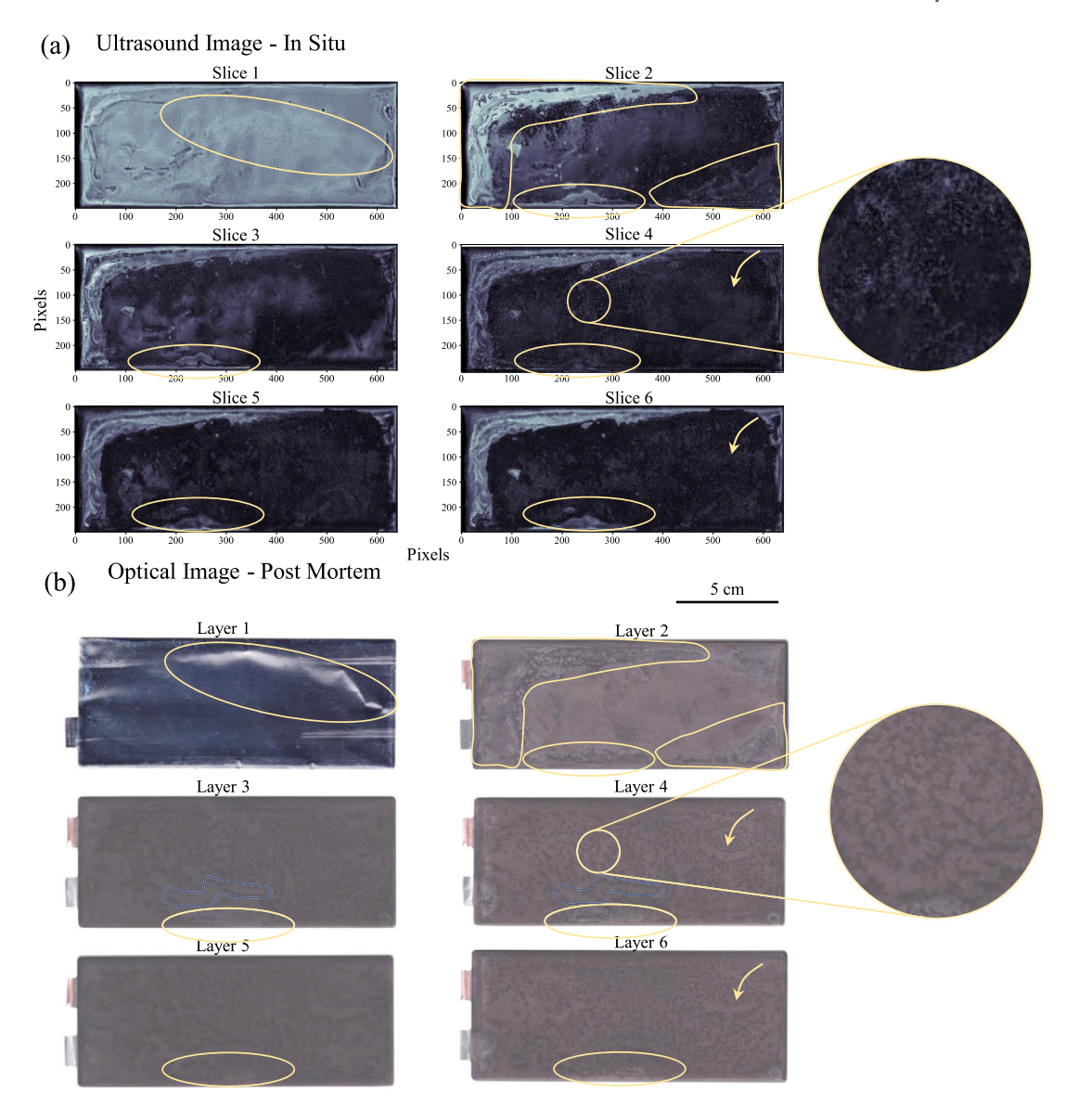


Fig. 4. Comparison between the generated ultrasound images and optical images from post-mortem analysis. (a) Represents each measurement point's first six calculated reflections (i.e., "slices"). (b) Shows the first six adjacent cathode and anode layers, which are superimposed semi-transparently. A selection of the similarities between the ultrasound and optical images is marked in yellow. The zoom highlights the detection of even small patterns of covering layers. The blue markers indicate structures that are visible with the altered algorithm that is depicted in the supplementary material. (For interpretation of the references to color in this figure legend, the reader is referred to the web version of this article.)

inside a battery cell reliably. The further markings show a selection of similarities between the ultrasound images and optical images. While some covering layers and other depositions can be imaged congruently, there are still some irregularities in the images which are not present in the optical images. There are multiple possible explanations for this. Firstly, the irregularities may be caused by the high covering layer thickness in some areas of the cell which, as will be shown in Section 5, is in the same order of magnitude as the electrode sheet thickness. This might distort the assignment of partial reflections to the electrode sheet in those areas, because of significant variance in distance between sensor and electrode, leading to a shorter time of flight. Secondly, a holistic variation of measurement parameters such as sensor frequency and bandwidth, focal point or coupling agent might help resolving this issue. Since the focus of this work is to present a methodology and demonstrate some of its possibilities, we leave this analysis for future publications. In addition to the proposed changes in the measurement setup, an alternative feature can be used to remove irregularities in the ultrasound image. Instead of calculating the reflection coefficient

(see Eq. (6)), we calculated the absolute value of the difference of two consecutive partial reflections. The feature was able to remove some of the irregularities in the generated images. Since the focus of this work is not to discuss these images in detail, they are shown in the supplementary material.

4.2. Images of the pristine cell

Finally, the ultrasound images of the pristine cell in Fig. 5 shall be analyzed as well. Although the cell is pristine, there are some inhomogeneities in the first slice of the ultrasound image. These are most probably caused by the packaging and direct contact from the separator and electrolyte to the aluminum current collector of the cathode (see Fig. 5(a)). Some of these inhomogeneities are also visible on the cathode current collector on the first layer of the optical post-mortem image (see Fig. 5(b)). The second slice shows few artifacts from the

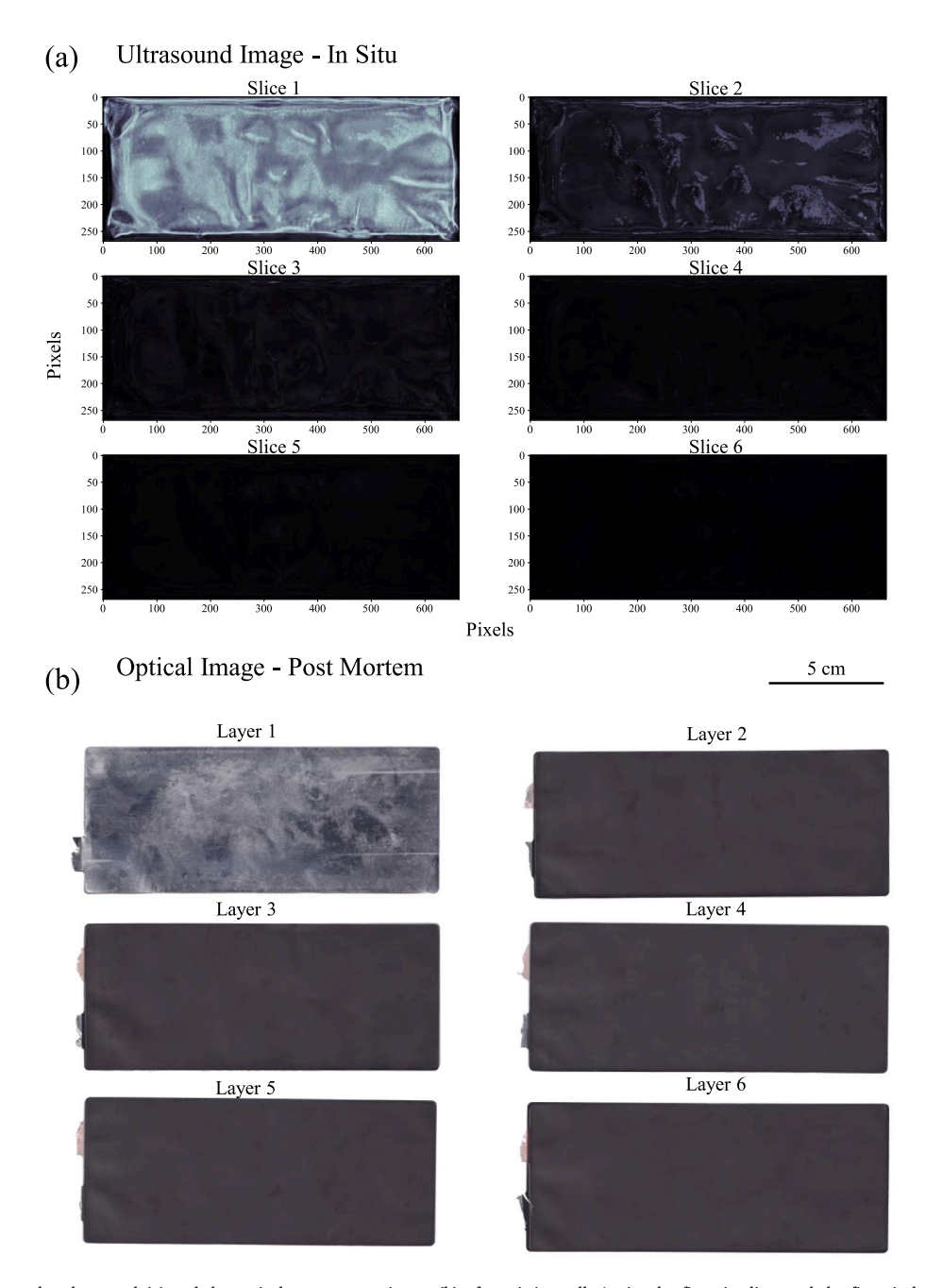


Fig. 5. Comparison between the ultrasound (a) and the optical post-mortem image (b) of a pristine cell. Again, the first six slices and the first six battery layers are compared. For the optical images, the first six adjacent cathode and anode layers are superimposed semi-transparently. Besides indications on the first slice and layer and possible artifacts on the second slice, the images are mostly identical.

calculation of the first slice. This error can be minimized with optimized parameterization of the calculation of the partial-reflection wavelets from Section 3.2.1. Since this artifact only occurs on the second slice and not on the subsequent ones and thus does not significantly deter the analysis, we leave this optimization to future publications. Besides these artifacts, the following slices are primarily homogeneous and match the optical images.

Therefore, there are clear differences to the aged cell. Especially no blurred pattern or any individual dots can be identified. For both cells, the same algorithms are applied to the images with identical color-map calculations to ensure comparability. This leads to the conclusion that the homogeneity of an ultrasound image can be a good predictor of the structural state of a battery.

5. Validation by post mortem analysis

Besides the already shown post-mortem scans with a flatbed scanner (Figs. 4 and 5), the electrode sheets from the aged cell were also examined using a laser scanning microscope (Keyence VK-X3000) and a scanning electron microscope (Zeiss Supra 55) in combination with an energy-dispersive X-ray spectroscopy detector (Oxford Xplore 30). Therefore 4 stamped samples with a diameter of 10 mm (Fig. 6) were punched out of the first and second anode sheets and will be referred to as stamp A to D.

All post-mortem analyses were performed under atmospheric exclusion. For this purpose, the laser scanning microscope is placed in the same argon-filled glove box (O_2 <5 ppm and H_2O <1 ppm) in which the cell opening took place. After the laser scanning measurement, the samples

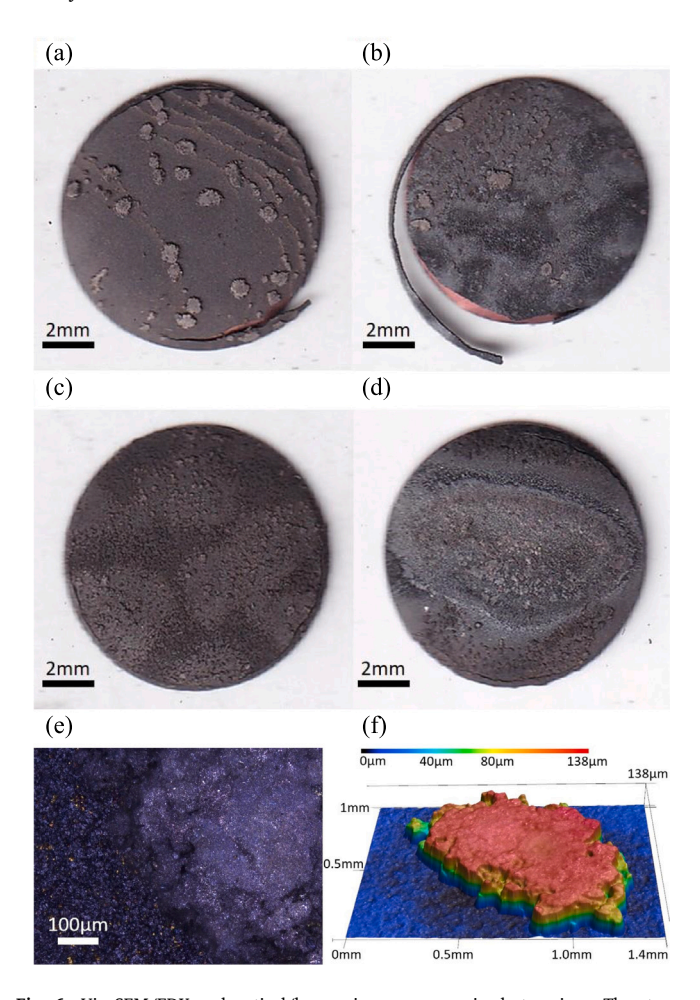


Fig. 6. Via SEM/EDX and optical/laser microscope examined stampings. The stamp positions on the electrode are shown in Fig. 4. The stamp depicted in subfigure (a) will be referred to as stamp A, the one in subfigure (b) as B etc. until (d). (e) and (f) are 2D and 3D laser scans of a large deposition on stamp A with the laser/optical microscope.

were transferred to the scanning electron microscope (SEM) using a transfer module (Kammrath & Weiss GmbH). This protects the samples from oxygen and/or moisture at all times, and no unwanted reaction with these during the transfer takes place.

In Fig. 6(e) and (f), an exemplary laser scanning image of a large deposition from stamp A is shown. The depositions have such a wide base that they are detectable even without a microscope (compare Fig. 6(a)). The color and structure of the deposition differ from the surrounding base material. For this base material, the typical graphite flake structure (see also Fig. 7(c)) and even some highly lithiated golden graphite particles are visible. The deposited material is more silver/grayish, and the mossy-like morphology is referred to in the literature as lithium plating [31]. With an area of approx. 0.7 mm x 1 mm and a height of up to 138 μ m, the deposits affect the ultrasonic signal and can be detected in the in situ ultrasound image due to their increased thickness, different morphology, and, therefore, acoustic impedance. For comparison, a typical (single-sided) graphite electrode thickness is in the range of 50–100 μ m, so that the depositions are thicker than the actual electrode coating [32].

To have a closer look at the deposits, the same stampings from the laser scanning microscope were used for the SEM investigation. In Fig. 7(a), an overview with marked focus spots of a deposition from stamp A is presented. Subfigure (b) displays a spot in the middle of the deposit, where a flattened surface consisting of a string/rod-like structure can be seen. This assumes that the deposit grows in rod/string islands until

the tip reaches the separator and is then flattened by it. Also, some mossy-like top layers on the string/rod-like structure can be seen. Here, it is assumed that the plated material reacts with parts of the electrolyte and forms a passivation layer. Subfigure (c) is a close-up view of the deposition edge. This structure is referred to in the literature as the "tree-like" plating morphology and will also be seen on other stamps (see Fig. 8(d)) [33]. The aforementioned spots depicted in Fig. 6(a-d) are closer examined in Figs. 7 and 8. Notably, Fig. 7(a) unveils a wide flat top on the islands, signifying their growth against a planar barrier, which can safely be assumed to be the separator. Moreover, the quantity and dimensions of these islands (measuring approximately 0.7 mm x 1 mm x 100um) surpass the expected size for salt deposits resulting from electrolyte evaporation. Even upon opening the cells, traces of electrolyte persisted on the electrode surface, gradually desiccating within a matter of seconds. Nevertheless, the intricate surface structures (as observed in Fig. 4) were promptly apparent upon cell opening, with residual electrolyte still present on the electrode. Furthermore, the electrodes underwent thorough washing in DMC (dimethyl carbonate) in an attempt to eliminate any remnants of electrolyte and conductive salt. Despite the rigorous washing process, all discernible structures remained intact, leading to the supposition that the observed surface deposits are indeed the result of Li-plating growth rather than residual salt precipitates. A closer look at the graphite material (Fig. 7(d)) shows small nano-size particles on top of the flake structure. Here, these small impurities are assumed to be lithium-plating seedlings that formed at the beginning of aging and then slowed down growing because a neighboring seedling grew faster [34]. To determine the elementary composition of the depositions, EDX measurements were performed. The results are displayed in the upper right corner of the SEM images in Fig. 7. The depositions consist mainly of fluorine and carbon, but high amounts of oxygen and phosphorus can be seen. It is assumed that the fluorine and phosphorus come from the reaction with LiPF₆ conductive salt. At the same time, single-digit mass fractions of sulfur were measured by EDX. Here it is assumed that sulfur-containing additives could be present in the electrolyte, which then react with the metallic lithium.

Fig. 8 summarizes the surfaces of stamps B, C, and D. Fig. 8(c) with a close-up window (d) taken from stamp C shows a similar surface like stamp A, except that the deposit is not as large as before and therefore not flattened at the top. Also, the already mentioned "tree-like" plating morphology of the deposit is well visible. Fig. 8(a) with a close-up window (b) from stamp B shows the "tree-like" agglomerates, with the difference that also the area in between is covered with medium height depositions. It is assumed that the initial deposition forming in this area was slower and, therefore, more homogeneous. In Fig. 8(e) with a close-up window (f) taken from stamp D, the 6-10 mm wide hill next to the current collector is seen. Similar to the depositions of stamp A, the surface is flattened by contact with the separator. Also, the already seen string/rod-like structure with additional surface depositions is visible, so here also, lithium plating, but with much larger dimensions, is assumed. Since the deposits can be seen all over the layers under consideration, it can be assumed that lithium plating has occurred along the entire surface, with an increased accumulation of plating at the edges of the cell.

6. Conclusion

Building on our previous work, we aimed to enable 3D imaging by developing an algorithm that dissects the ultrasound data to create layer-specific depth resolution. This was achieved by analyzing the reflected instead of the transmitted ultrasound wave. The algorithm was split into two main tasks allowing a modular implementation of the imaging methods. In the first step, the individual reflections at each electrode were approximated, considering the overlapping of reflections due to the limited bandwidth of ultrasound sensors and thin-layered cell structure. In the second step, we calculated the reflection

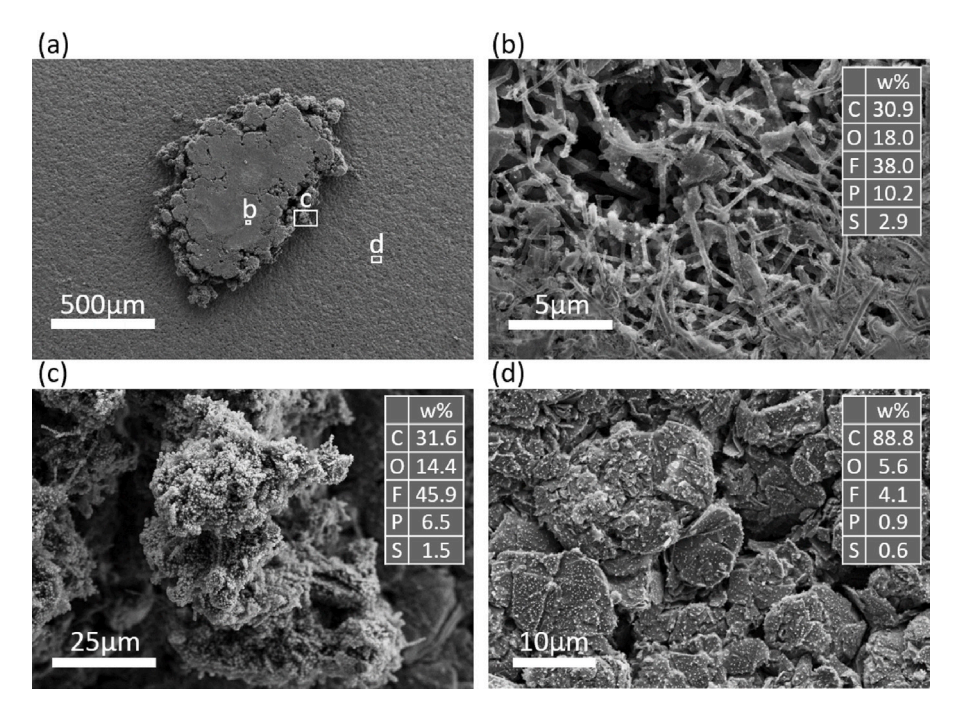


Fig. 7. SEM images with various magnifications and focus spots on stamp A (Fig. 6). The positions of the scan fields (b), (c) and (d) are marked in the overview image (a).

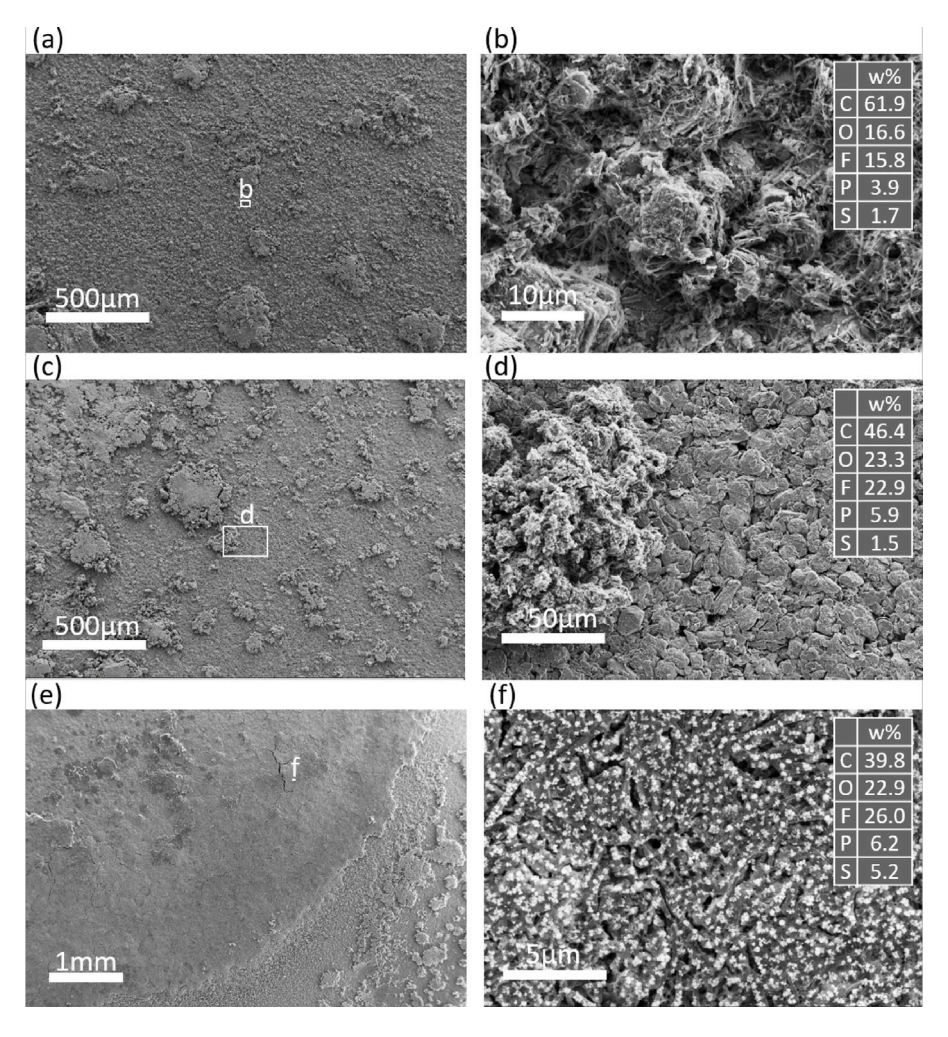


Fig. 8. SEM images with various magnifications of stamp B (a)/(b), C (c)/(d) and D (e)/(f) (Fig. 6).

coefficient of each layer transition and mapped it on a color map. We applied this procedure to two different cells: An aged and a pristine pouch cell from the manufacturer Kokam. The ultrasound images were compared to optical images from a post-mortem analysis. For the aged cell, clear indications of internal structural inhomogeneities were visible and separated layer by layer. These indications were visible in the optical images as well. In a post-mortem analysis, these were identified as lithium-plating and gassing. For the pristine cell, no indications were visible on the ultrasound images. The post-mortem analysis revealed no structural inhomogeneities on the optical images of the cell. While the proposed method generated images that revealed a spatially resolved correlation with the local aging phenomena, future work should focus on a parameter variation of the measurement equipment, such as sensor frequency, bandwidth, or focal point, to make the resulting ultrasound images more congruent with the optical images, even on deeper layers. Since our methods focused on qualitative indications of local aging phenomena, it is of interest to combine the methods with quantitative measurements of mechanical properties, such as the Young's modulus, to enable a comprehensive mechanical analysis of the cell under investigation. Furthermore, the ultrasound data suggests that enabling a more robust gas detection is possible based on the acoustic response's characteristics. Since the measurements in this publication are based on the reflected ultrasound wave, it remains an open question whether layer resolution is achievable using the transmitted ultrasound wave. While this would, by design, enable full 3D imaging of the specimen, it might be a great challenge to engineer the suitable sensor and measurement equipment to non-destructive image the entire cell while keeping a small ultrasound wavelength. Since acoustic responses are currently interpreted visually, it would be of great interest in the future to generate a model that can verify effects such as gassing and deposit formation without subsequent post-mortem analysis. We are convinced this publication will enable researchers to detect structural inhomogeneities in 3D and, therefore, serve as a scalable verification method for research and development of future battery cells.

CRediT authorship contribution statement

David Wasylowski: Project administration, Supervision, Conceptualisation, Methodology, Software, Investigation, Data curation, Validation, Writing – original draft, Visualisation. Sven Neubauer: Software, Formal analysis, Writing – original draft, Visualisation. Matthias Faber: Data curation, Writing – original draft, Resources. Heinrich Ditler: Data curation, Writing – original draft. Morian Sonnet: Software, Data curation. Alexander Blömeke: Methodology, Writing – review & editing, Funding acquisition. Philipp Dechent: Methodology, Writing – review & editing. Alexander Gitis: Conceptualisation. Dirk Uwe Sauer: Supervision, Funding acquisition.

Declaration of competing interest

The authors declare that they have no known competing financial interests or personal relationships that could have appeared to influence the work reported in this paper.

Data availability

Data will be made available on request.

Acknowledgments

This work was funded by the Federal Ministry of Education and Research as part of the research cluster "Batterienutzungskonzepte" through the project MADAM4Life (grant number 03XP0327C) and NUBase (grant number 03XP0322C) and as part of the research cluster "AQua" through the project InOPlaBat (grant number 03XP0352A).

Appendix A. Supplementary data

Supplementary material related to this article can be found online at https://doi.org/10.1016/j.jpowsour.2023.233295.

References

- [1] Y. Zhao, O. Pohl, A.I. Bhatt, G.E. Collis, P.J. Mahon, T. Rüther, A.F. Hollenkamp, A review on battery market trends, second-life reuse, and recycling, Sustain. Chem. 2 (1) (2021) 167–205, http://dx.doi.org/10.3390/suschem2010011, URL https://www.mdpi.com/2673-4079/2/1/11.
- [2] L. Usai, J.J. Lamb, E. Hertwich, O.S. Burheim, A.H. Strømman, Analysis of the li-ion battery industry in light of the global transition to electric passenger light duty vehicles until 2050, Environ. Res. Infrastructure Sustain. 2 (1) (2022) 011002, http://dx.doi.org/10.1088/2634-4505/ac49a0.
- [3] G. Lenze, H. Bockholt, C. Schilcher, L. Froböse, D. Jansen, U. Krewer, A. Kwade, Impacts of variations in manufacturing parameters on performance of lithiumion-batteries, J. Electrochem. Soc. 165 (2) (2018) A314–A322, http://dx.doi.org/ 10.1149/2.1081802ies.
- [4] M. Wolter, G. Fauser, C. Bretthauer, M.A. Roscher, End-of-line testing and formation process in Li-ion battery assembly lines, in: International Multi-Conference on Systems, Signals & Devices, 2012, pp. 1–3, http://dx.doi.org/10. 1109/SSD.2012.6198092.
- [5] T. Kornas, E. Knak, R. Daub, U. Bührer, C. Lienemann, H. Heimes, A. Kampker, S. Thiede, C. Herrmann, A multivariate KPI-based method for quality assurance in lithium-ion-battery production, Procedia CIRP 81 (2019) 75–80, http://dx.doi.org/10.1016/j.procir.2019.03.014, URL https://www.sciencedirect.com/science/article/pii/S2212827119303191. 52nd CIRP Conference on Manufacturing Systems (CMS), Ljubljana, Slovenia, June 12-14, 2019.
- [6] Z. Yu, H. Shan, Y. Zhong, X. Zhang, G. Hong, Leveraging advanced X-ray imaging for sustainable battery design, ACS Energy Lett. 7 (9) (2022) 3151–3176, http://dx.doi.org/10.1021/acsenergylett.2c01297.
- [7] D. Atkins, E. Capria, K. Edström, T. Famprikis, A. Grimaud, Q. Jacquet, M. Johnson, A. Matic, P. Norby, H. Reichert, J.-P. Rueff, C. Villevieille, M. Wagemaker, S. Lyonnard, Accelerating battery characterization using neutron and synchrotron techniques: toward a multi-modal and multi-scale standardized experimental workflow, Adv. Energy Mater. 12 (17) (2022) 2102694, http://dx.doi.org/10.1002/aenm.202102694, URL https://onlinelibrary.wiley.com/doi/abs/10.1002/aenm.202102694. eprint: https://onlinelibrary.wiley.com/doi/pdf/10.1002/aenm.202102694.
- [8] N. Sharp, P. ORegan, D. Adams, J. Caruthers, A. David, M. Suchomel, Lithiumion battery electrode inspection using pulse thermography, NDT E Int. 64 (2014) 41–51, http://dx.doi.org/10.1016/j.ndteint.2014.02.006, URL https:// www.sciencedirect.com/science/article/pii/S0963869514000346.
- [9] A.J. Ilott, M. Mohammadi, H.J. Chang, C.P. Grey, A. Jerschow, Real-time 3D imaging of microstructure growth in battery cells using indirect MRI, Proc. Natl. Acad. Sci. 113 (39) (2016) 10779–10784, http://dx.doi.org/ 10.1073/pnas.1607903113, arXiv:https://www.pnas.org/doi/pdf/10.1073/pnas. 1607903113. URL https://www.pnas.org/doi/abs/10.1073/pnas.1607903113.
- [10] W. Chang, R. May, M. Wang, G. Thorsteinsson, J. Sakamoto, L. Marbella, D. Steingart, Evolving contact mechanics and microstructure formation dynamics of the lithium metal-Li7La3Zr2O12 interface, Nature Commun. 12 (1) (2021) http://dx.doi.org/10.1038/s41467-021-26632-x.
- [11] Z. Deng, X. Lin, Z. Huang, J. Meng, Y. Zhong, G. Ma, Y. Zhou, Y. Shen, H. Ding, Y. Huang, Recent progress on advanced imaging techniques for lithium-ion batteries, Adv. Energy Mater. 11 (2) (2020) 2000806, http://dx.doi.org/10.1002/aenm.202000806.
- [12] D. Zhe, H. Zhenyu, L. Lei, H. Yunhui, S. Yue, Applications of ultrasound technique in characterization of lithium-ion batteries, Energy Storage Sci. Technol. 8 (6) (2019) 1033, http://dx.doi.org/10.12028/j.issn.2095-4239.2019.0146, URL https://esst.cip.com.cn/EN/abstract/article_965.shtml.
- [13] Z. Deng, Z. Huang, Y. Shen, Y. Huang, H. Ding, A. Luscombe, M. Johnson, J.E. Harlow, R. Gauthier, J.R. Dahn, Ultrasonic scanning to observe wetting and "unwetting" in Li-Ion pouch cells, Joule 4 (9) (2020) 2017–2029, http: //dx.doi.org/10.1016/j.joule.2020.07.014.
- [14] D. Wasylowski, N. Kisseler, H. Ditler, M. Sonnet, G. Fuchs, F. Ringbeck, D.U. Sauer, Spatially resolving lithium-ion battery aging by open-hardware scanning acoustic imaging, J. Power Sources 521 (2022) 230825, http://dx.doi.org/10.1016/j.jpowsour.2021.230825.
- [15] L.P. Bauermann, L. Mesquita, C. Bischoff, M. Drews, O. Fitz, A. Heuer, D. Biro, Scanning acoustic microscopy as a non-destructive imaging tool to localize defects inside battery cells, J. Power Sources Adv. 6 (2020) 100035, http://dx.doi.org/10.1016/j.powera.2020.100035.
- [16] S. Feiler, P. Daubinger, L. Gold, S. Hartmann, G.A. Giffin, Interplay between elastic and electrochemical properties during active material transitions and aging of a lithium-Ion battery, Batter. Supercaps 6 (4) (2023) e202200518, http: //dx.doi.org/10.1002/batt.202200518, URL https://onlinelibrary.wiley.com/doi/ abs/10.1002/batt.202200518. _eprint: https://onlinelibrary.wiley.com/doi/pdf/ 10.1002/batt.202200518.

- [17] P. Ladpli, C. Liu, F. Kopsaftopoulos, F.-K. Chang, Estimating lithium-ion battery state of charge and health with ultrasonic guided waves using an efficient matching pursuit technique, in: 2018 IEEE Transportation Electrification Conference and Expo, Asia-Pacific, ITEC Asia-Pacific, 2018, pp. 1–5, http://dx.doi.org/10. 1109/ITEC.AP 2018 8432327
- [18] M. Huang, N. Kirkaldy, Y. Zhao, Y. Patel, F. Cegla, B. Lan, Quantitative characterisation of the layered structure within lithium-ion batteries using ultrasonic resonance, J. Energy Storage 50 (2022) 104585, http://dx.doi.org/ 10.1016/j.est.2022.104585, URL https://www.sciencedirect.com/science/article/ pii/S2352152X22006016.
- [19] M. Lewerenz, J. Münnix, J. Schmalstieg, S. Käbitz, M. Knips, D.U. Sauer, Systematic aging of commercial LiFePO4|Graphite cylindrical cells including a theory explaining rise of capacity during aging, J. Power Sources 345 (2017) 254-263, http://dx.doi.org/10.1016/j.jpowsour.2017.01.133, URL https://www. sciencedirect.com/science/article/pii/S037877531730143X.
- [20] K. Sakai, O. Kikuchi, K. Kitami, M. Umeda, S. Ohno, Defect detection method using statistical image processing of scanning acoustic tomography, in: 2016 IEEE 23rd International Symposium on the Physical and Failure Analysis of Integrated Circuits, IPFA, IEEE, 2016, http://dx.doi.org/10.1109/ipfa.2016.7564303.
- [21] Z. Deng, Z. Huang, Y. Shen, Y. Huang, H. Ding, A. Luscombe, M. Johnson, J.E. Harlow, R. Gauthier, J.R. Dahn, Ultrasonic scanning to observe wetting and "unwetting" in li-ion pouch cells, Joule 4 (9) (2020) 2017–2029, http: //dx.doi.org/10.1016/j.joule.2020.07.014, URL https://www.sciencedirect.com/ science/article/pii/S2542435120303329.
- [22] Y. Qi, H. Guo, L.G. Hector, A. Timmons, Threefold increase in the Young's modulus of graphite negative electrode during lithium intercalation, J. Electrochem. Soc. 157 (5) (2010) A558, http://dx.doi.org/10.1149/1.3327913, URL https://iopscience.iop.org/article/10.1149/1.3327913/meta. Publisher: IOP Publishing.
- [23] G.Y. Gor, J. Cannarella, J.H. Prévost, C.B. Arnold, A model for the behavior of battery separators in compression at different strain/charge rates, J. Electrochem. Soc. 161 (11) (2014) F3065, http://dx.doi.org/10.1149/2.0111411jes, URL https://iopscience.iop.org/article/10.1149/2.0111411jes/meta. Publisher: IOP Publishing.
- [24] Z. Luo, X. Li, J. Shang, H. Zhu, D. Fang, Modified rule of mixtures and Halpin–Tsai model for prediction of tensile strength of micron-sized reinforced composites and Young's modulus of multiscale reinforced composites for direct extrusion fabrication, Adv. Mech. Eng. 10 (7) (2018) 1687814018785286, http: //dx.doi.org/10.1177/1687814018785286, Publisher: SAGE Publications.

- [25] L.B. Freund, S. Suresh, Thin film materials: Stress, defect formation and surface evolution, 2004, Cambridge Core. URL https://www.cambridge.org/ core/books/thin-film-materials/9DC3055061A07C92A6A9D83CBF804029. ISBN: 9780521822817 9780521529778 9780511754715 Publisher: Cambridge University Press. http://dx.doi.org/10.1017/CBO9780511754715.
- [26] R.O.E. Vijgen, J.H. Dautzenberg, Mechanical measurement of the residual stress in thin PVD films, 22nd International Conference on Metallurgical Coatings and Thin Films, Thin Solid Films 270 (1) (1995) 264–269, http://dx.doi.org/10.1016/ 0040-6090(95)06984-4, URL https://www.sciencedirect.com/science/article/pii/ 0040609095069844.
- [27] M. Huang, N. Kirkaldy, Y. Zhao, Y. Patel, F. Cegla, B. Lan, Quantitative characterisation of the layered structure within lithium-ion batteries using ultrasonic resonance, J. Energy Storage 50 (2022) 104585.
- [28] A.A. Assef, J. de Oliveira, J.M. Maia, E.T. Costa, FPGA implementation and evaluation of an approximate Hilbert transform-based envelope detector for ultrasound imaging using the DSP builder development tool, in: 2019 41st Annual International Conference of the IEEE Engineering in Medicine and Biology Society, EMBC, 2019, pp. 2813–2816, http://dx.doi.org/10.1109/EMBC.2019. 8857671
- [29] P.J. Brands, A.P. Hoeks, L.A. Ledoux, R.S. Reneman, A radio frequency domain complex cross-correlation model to estimate blood flow velocity and tissue motion by means of ultrasound, Ultrasound Med. Biol. 23 (6) (1997) 911–920, http: //dx.doi.org/10.1016/S0301-5629(97)00021-5, URL https://www.sciencedirect. com/science/article/pii/S0301562997000215.
- [30] S. Weinzierl, Handbuch der Audiotechnik Grundlagen, in: Handbuch Der Audiotechnik, 2008, pp. 1–39.
- [31] F. Ringbeck, C. Rahe, G. Fuchs, D.U. Sauer, Identification of lithium plating in lithium-ion batteries by electrical and optical methods, J. Electrochem. Soc. 167 (9) (2020) 090536.
- [32] Y. Zheng, L. Pfäffl, H.J. Seifert, W. Pfleging, Lithium distribution in structured graphite anodes investigated by laser-induced breakdown spectroscopy, Appl. Sci. 9 (20) (2019) 4218.
- [33] H. Kühnle, E. Knobbe, E. Figgemeier, In situ optical investigations of lithium depositions on pristine and aged lithium metal electrodes, J. Electrochem. Soc. 168 (2) (2021) 020510.
- [34] H. Liu, X. Cheng, R. Zhang, P. Shi, X. Shen, X. Chen, T. Li, J. Huang, Q. Zhang, Mesoporous graphene hosts for dendrite-free lithium metal anode in working rechargeable batteries. Trans. Tianjin Univ. 26 (2) (2020) 127–134.